MDPI

Article

Highly Ordered TiO₂ Nanotube Arrays with Engineered Electrochemical Energy Storage Performances

Wangzhu Cao [1], Kunfeng Chen [1,*] and Dongfeng Xue [1,2,*]

1   State Key Laboratory of Crystal Materials, Institute of Crystal Materials, Shandong University, Jinan 250100, China; caowangzhu@sdu.edu.cn
2   Shenzhen Institute of Advanced Electronic Materials, Shenzhen Institutes of Advanced Technology, Chinese Academy of Sciences, Shenzhen 518055, China
*   Correspondence: Kunfeng.Chen@sdu.edu.cn (K.C.); df.xue@siat.ac.cn (D.X.)

Abstract: Nanoscale engineering of regular structured materials is immensely demanded in various scientific areas. In this work, vertically oriented TiO₂ nanotube arrays were grown by self-organizing electrochemical anodization. The effects of different fluoride ion concentrations (0.2 and 0.5 wt% NH₄F) and different anodization times (2, 5, 10 and 20 h) on the morphology of nanotubes were systematically studied in an organic electrolyte (glycol). The growth mechanisms of amorphous and anatase TiO₂ nanotubes were also studied. Under optimized conditions, we obtained TiO₂ nanotubes with tube diameters of 70–160 nm and tube lengths of 6.5–45 μm. Serving as free-standing and binder-free electrodes, the kinetic, capacity, and stability performances of TiO₂ nanotubes were tested as lithium-ion battery anodes. This work provides a facile strategy for constructing self-organized materials with optimized functionalities for applications.

Keywords: TiO₂; crystal growth; Li-ion batteries; nanotube array; anodization

1. Introduction

Since titanium dioxide (TiO₂) was first used in the electrochemical photolysis of water in 1972, researchers have developed a strong interest in TiO₂ [1–4]. TiO₂ exhibits rich physical and chemical properties such as non-toxicity, high corrosion resistance, biocompatibility, and unique optoelectronic properties, allowing it to maintain good competitiveness in photocatalysis, sensors, dye-sensitized solar cells, and electrochemical energy storage, etc. [5–11]. After decades of development, nanoscale materials (0D, 1D, 2D, and 3D) are becoming key in controlling various performances [12]. Among these nanomaterials, 1D nanotubes have received more and more attention in the materials field. After the synthesis of carbon nanotubes, the research on highly ordered nanotube structures aroused a great upsurge of interest [13–15]. Research on TiO₂ nanotubes has also became a hot spot.

Three methods can be used for preparing TiO₂ nanotubes: the template method [16], the hydrothermal (solvothermal) method [17], and the electrochemical anodization method [18]. For the template method, TiO₂ nanotubes have a larger inner diameter and thicker tube wall, and their morphology is restricted by the template. With the hydrothermal (solvothermal) way, TiO₂ nanotubes have small tube diameters, thin tube walls, and their morphology is also difficult to control. Of these methods, the anodic oxidation method displays the simplest operation process and has the advantages of vertical arrangement and highly ordered nanotube arrays [19,20]. The preparation technology of anodized TiO₂ nanotube arrays can be roughly divided into three generations: (i) hydrofluoric acid aqueous electrolyte was used in the first generation, and the length of obtained nanotubes was only 500 nm [21]; (ii) F⁻-containing water-based electrolyte was applied, and the length of the nanotubes was 5 μm [22]; (iii) F⁻-containing organic electrolytes were used, and the length of the nanotubes reached 100–1000 μm, while the nanotubes were smooth and better than those of the previous two generations [23].

Numerous research efforts have been made to study the influencing factors of self-ordered TiO_2 nanotube structures; i.e., F^- concentration, pH value, water content, type of electrolyte, oxidation voltage, oxidation time, and reaction temperature [24]. The concentration of F^- ions must be kept at a proper level to achieve the balance between growth and dissolution of nanotubes [25]. With HF acidic electrolytes, only 5 μm-long nanotubes were produced [19]. In a fluoride salt solution, the chemical dissolution rate of TiO_2 reduced and 24 μm-long nanotubes can be obtained [23]. F^- ions are more aggressive in aqueous solutions than in organic media; typically side walls of the nanotubes appear distorted in water, while they grow more smoothly in organic solutions [26]. The lower water content in organic electrolytes increases the growth rate of the nanotubes [27]. The applied potential affects the migration of ions and the morphology of the nanotubes, which is often 5–30 V in water electrolyte and 10–60 V in organic electrolytes [28]. In organic electrolytes, the optimal temperature range for nanotubes growth was shown to be between 0 and 40 °C [29]. However, there still exist less known but important aspects to be explored, such as the fundamentals of nanotube growth, the effect of defects in the Ti substrate, the effect of heat-treatments, the improvements in the applications of nanotubes, etc.

Vertically oriented self-organized TiO_2 nanotubes have become an excellent candidate material for lithium-ion battery anodes. The benefits of TiO_2 nanotube arrays are shown as follows [30–32]: (i) Good structural stability, large specific surface area, small volume expansion rate. (ii) With a hollow tubular structure, the gaps between tubes are conducive to the penetration of the electrolyte. The inner and outer walls of the tube increase the contact area between the electrode and the electrolyte, shorten the diffusion path of lithium ions, and facilitate the reversible insertion/extraction of lithium ions. (iii) The active materials are firmly combined with the metal titanium matrix, without the need to add additional binders and conductive agents. (iv) As a negative electrode, the high voltage can avoid the precipitation of metallic lithium, so it is a promising candidate as a safe lithium-ion battery anode material.

In this work, we revisited the so-called "old field" of anodic oxidation and finding an inherent mechanism for engineering regular nanotube structured materials with electrical and chemical fields to improve the areal capacity, rate capability, and cycling stability of lithium-ion battery anodes, and fabrication strategies for TiO_2 nanotube electrodes were systematically optimized.

2. Experimental Section

2.1. Reagents and Materials

Titanium foil (99.99%, Qinghe Shenghang Metal Material Co. Ltd., Shanghai, China); platinum electrode (99.99%, Shanghai Yueci Electronic Technology Co. Ltd., Shanghai, China); ethylene glycol (EG, 99.5%, Sinopharm Chemical Reagent Co. Ltd., Shanghai, China); ammonium fluoride (NH_4F, 96.0%, Tianjin Komiou Chemical Reagent Co. Ltd., Tianjin, China); anhydrous ethanol (99.7%, Tianjin Fuyu Fine Chemical Co. Ltd., Tianjin, China).

2.2. Preparation of TiO2 Nanotube Arrays

The high-purity titanium foil (10 mm × 35 mm × 0.1 mm) was ultrasonically cleaned with anhydrous ethanol and deionized water for 10 min, respectively. Then, titanium foil was dried in the air. One side of dried titanium foil was sealed with insulating tape. As shown in Figure 1, a two-electrode system was used, and a high-purity platinum foil (15 mm × 15 mm × 0.1 mm) was used as a counter electrode. The two electrodes had a distance of 2 cm. Electrolytes were prepared with 75 mL EG, 0.5 wt% NH_4F and 757 μL deionized water. In another set of experiments, 0.2 wt% NH_4F was used, and other conditions remained unchanged. At 20 °C, a DC power supply (NPS3010W, Wanptek, Shenzhen, China) was used to provide a constant voltage potential of 60 V, and oxidation time was 2, 5, 10, and 20 h, respectively. After reaction, the titanium foil was taken out and cut into 3 sheets of 10 mm × 10 mm. Then, ultrasonic cleaning was conducted with EG

and anhydrous ethanol for 10 min, respectively, and we then rinsed the sheets lightly with anhydrous ethanol three times. Finally, we removed the back insulating tape and dried the sheets in the air.
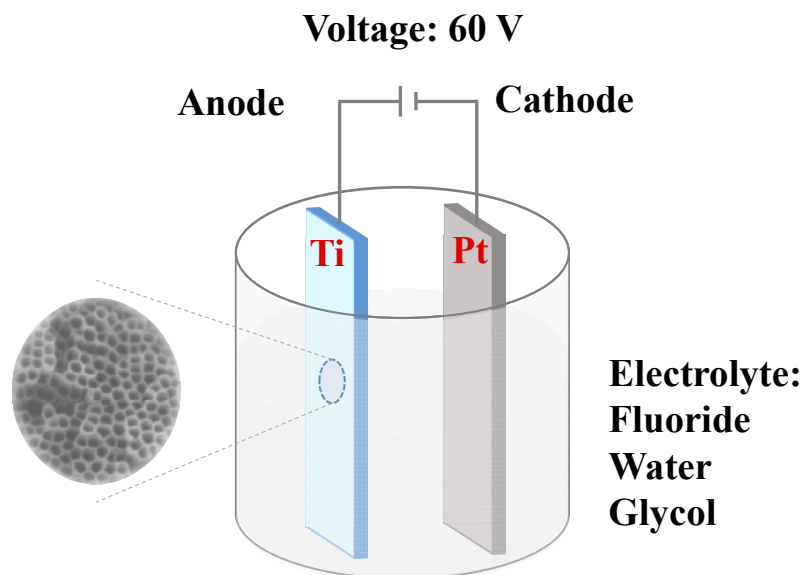

Figure 1. Schematic illustration of an electrochemical anodic oxidation cell.

As for the annealing steps, the prepared TiO_2 nanotube array was first placed in a quartz boat and then transferred to the programmed temperature-controlled muffle furnace. Then, it was held at 450 °C for two hours with a heating rate of 5 °C per minute. After temperature decreased to room temperature, the annealed sample was taken out. The sample name of TiO_2-5 h-450 °C denoted a sample anodized for 5 h and heated at 450 °C. TiO_2-5 h denoted a sample anodized for 5 h before annealing.

2.3. Electrochemical Analysis of Li/TiO$_2$ Cells

In a glove box filled with Ar, the Li/TiO_2 cells were assembled into 2032 coin batteries. A glass microfiber separator was put between the electrode and the lithium sheet, and the separator was fully wetted with 1 M liquid electrolyte $LiPF_6$ dissolved in a 1:1 volume ratio of dimethyl carbonate (DMC) and ethylene carbonate (EC). In this work, the Li/TiO_2 cells were tested with charge–discharge equipment (Lanhe CT3001A, Wuhan, China) at a series of current densities within the voltage range of 1–3 V (vs. Li/Li^+). Cyclic voltammograms (CV) and electrochemical impedance spectroscopy were conducted at an electrochemical workstation (CHI 660E, Shanghai, China).

2.4. Characterization

The samples were investigated by X-ray diffraction (XRD, Rigaku, SmartLab 9KW, Tokyo, Japan), scanning electron microscopy (SEM, JEOL, JSM-6700F, Tokyo, Japan) and UV laser confocal Raman Spectrometer (Horiba, LabRAM HR Evolution, 532 laser, 100–1000 cm^{-1}, Paris, France). The XRD test parameters were: Cu target, Kα λ = 0.154056 nm, the scanning speed was 20° per minute, the scanning step was 0.01°, and the scanning range was 10–90°.

3. Results and Discussion

The process of anodizing and growing TiO_2 nanotube arrays in F^- ions containing organic electrolytes was separated into four stages. **In the first stage**, a layer of dense TiO_2 barrier layer was rapidly generated at the anode after voltage was applied (Figure 2a). In this stage, H_2O was ionized into H^+ cations and O^{2-} anions (Figure 2, Formula (i)). At the same time, metal titanium was dissolved into Ti^{4+} cations (Figure 2, Formula (ii)), and then a large number of Ti^{4+} cations combined with O^{2-} anions to form a dense TiO_2

film (Figure 2, Formula (iii)). The overall reaction can be summarized as Formula (iv) in Figure 2 [33]. **In the second stage**, F^- ions chemically etched the barrier layer to produce a large number of pits (Figure 2b); as the barrier layer continued to penetrate into the titanium substrate, the pits became larger and nanopores appeared (Figure 2c). The formation of a dense oxide layer resulted in volume expansion and generated internal stress. Then, the F^- ions reacted with the TiO_2 barrier layer and chemical etching occurred: the chemical dissolution of oxides (Figure 2, Formula (vi)) or the direct complexation of the free Ti^{4+} cations (Figure 2, Formula (v)). A large number of pits on the oxide layer were found (Figure 3a) and these pits were the precursors of pores (Figure 3b) [34].
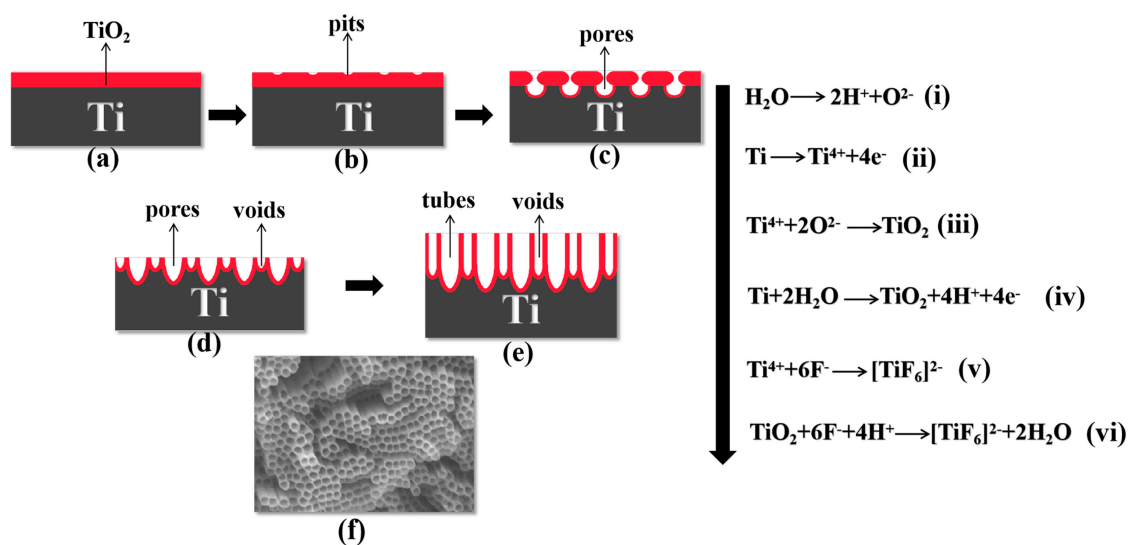

$$H_2O \longrightarrow 2H^+ + O^{2-} \quad (i)$$

$$Ti \longrightarrow Ti^{4+} + 4e^- \quad (ii)$$

$$Ti^{4+} + 2O^{2-} \longrightarrow TiO_2 \quad (iii)$$

$$Ti + 2H_2O \longrightarrow TiO_2 + 4H^+ + 4e^- \quad (iv)$$

$$Ti^{4+} + 6F^- \longrightarrow [TiF_6]^{2-} \quad (v)$$

$$TiO_2 + 6F^- + 4H^+ \longrightarrow [TiF_6]^{2-} + 2H_2O \quad (vi)$$

Figure 2. Schematic diagram of nanotube evolution at constant anodization voltage: (**a**) formation of TiO_2 barrier layer; (**b**) pits formed on the oxide layer; (**c**) pits growing into pores morphology; (**d**) pores' growth and voids' formation; (**e**) formation of TiO_2 nanotubes; (**f**) top view of fully grown TiO_2 nanotube arrays. Formulas (i)–(vi) are the chemical reactions that occurred during the anodic oxidation process.
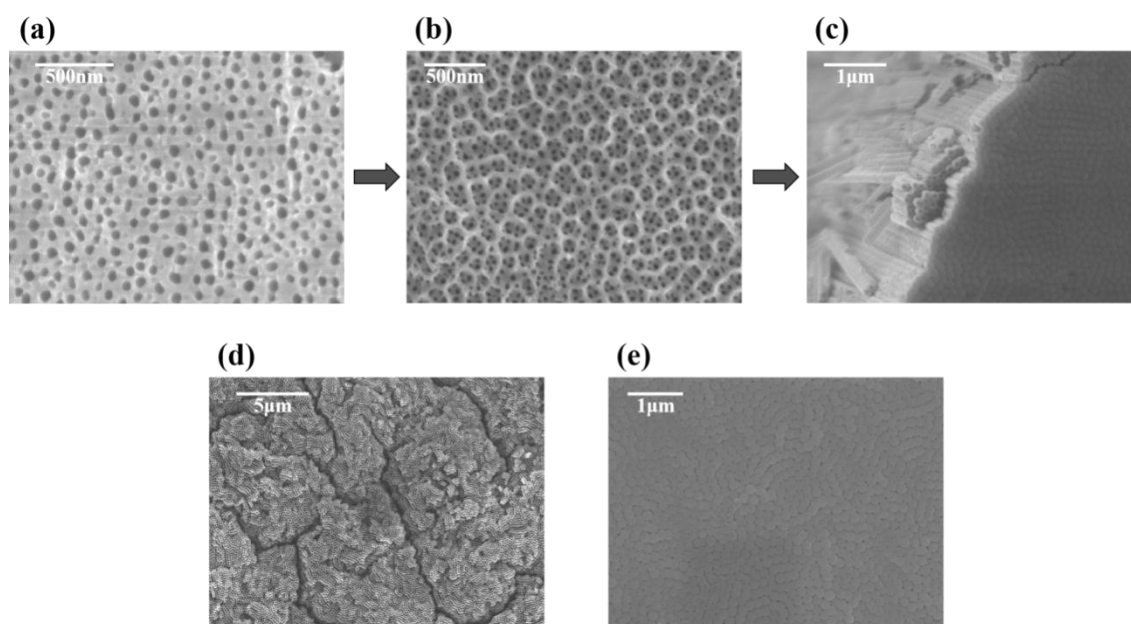

Figure 3. SEM images showing growth process of TiO_2 nanotube array: (**a**) pits formed on the oxide layer; (**b**) conversion of pits to nanopores; (**c**) conversion of nanopores to nanotubes; (**d**) the top view of the nanotube array; (**e**) the bottom view of the nanotube array.

In the third stage, the porous membrane began to grow steadily and form TiO_2 nanotubes (Figure 2d,e and Figure 3c). As the pores extended to the titanium substrate, the electric field intensity of the metal region increased, accelerating the growth and dissolution rate of the oxide film. Simultaneously, stress corrosion occurred between adjacent nanopores, which created voids at the interface of the pores. Due to the growth stresses, pores were formed as a consequence of flow of material in the oxide barrier layer under the porous layer toward the wall regions and field-assisted plasticity of the film material [27]. With the nanopores continuing to grow, the joints between pores continued to extend to the titanium substrate, eventually forming the tube wall [35]. The formation of dynamic equilibrium between the oxidation reaction at the oxide/titanium substrate interface (Figure 2, Formula (iv)) and the dissolution reaction at the electrolyte/oxide interface (Figure 2, Formulas (v) and (vi)) led to the development of TiO_2 nanotubes [36]. The top and bottom of the nanotube array are exhibited in Figure 3d,e. **In the final stage**, when the dissolution rate of TiO_2 nanotubes on the top was equal to the growth rate of the nanotubes, the reaction entered the equilibrium stage, at which time the length of the nanotubes no longer increased [33].

Figure 4a shows XRD patterns of as-obtained amorphous TiO_2 and annealed TiO_2 at 450 °C for 2 h. Before annealing, only the characteristic diffraction peaks of Ti substrate at 34.9, 38.2, 40.0, 52.8, 62.8, 70.5, 76.0, 82.1 and 86.6° existed. After annealing, the characteristic diffraction peaks at 25.2, 36.9, 42.9, 53.8, 54.9, 68.6 and 74.9° belonged to the anatase TiO_2 phase. The TiO_2 nanotubes obtained by anodizing for 2, 5, 10, and 20 h had the same crystal structure. The results show that oxidation time had no influence on the crystal phase of samples. Furthermore, Raman spectra were performed to study their structures (Figure 4b). According to group theory analysis of anatase TiO_2, there were six optical vibration modes of anatase TiO_2 with Raman activity, which were one A_{1g}, two B_{1g}, and three E_g modes respectively. As shown in Figure 4b, five peaks of anatase TiO_2 were observed. The peak positions and vibration modes were 140 cm^{-1}, E_{g1}; 193 cm^{-1}, E_{g2}; 391 cm^{-1}, $B_{1g(1)}$; 511 cm^{-1}, $A_{1(g)} + B_{1g(2)}$, and 633 cm^{-1}, E_{g3}, respectively. This result is consistent with the previously reported pure anatase TiO_2 structure [37].
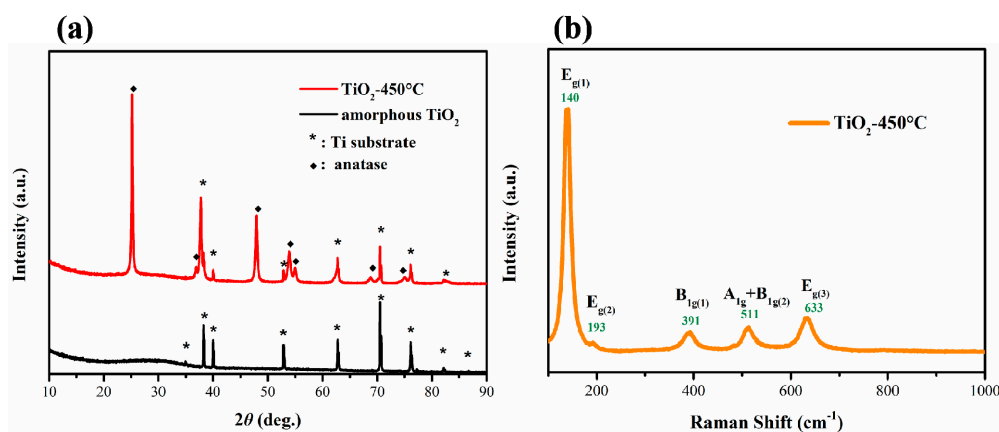

Figure 4. (**a**) XRD patterns of amorphous TiO_2-20 h and anatase TiO_2-20 h-450 °C. (**b**) Raman spectra of anatase TiO_2 nanotubes after annealing. The samples were synthesized in electrolyte with 0.5 wt% NH_4F and with anodization oxidation time of 20 h.

Figure 5 shows SEM images of TiO_2 nanotube arrays before and after annealing with different oxidation times at 0.2 wt% NH_4F. The diameters and lengths of TiO_2 nanotubes were: 70 nm and 6.5 μm in 2 h oxidation (Figure 5a); 100 nm and 11 μm in 5 h oxidation (Figure 5b); 130 nm and 17 μm in 10 h oxidation (Figure 5c); and 145 nm and 40 μm in 20 h oxidation (Figure 5d), respectively. The above changes clearly demonstrate the transformation process from nanopores to nanotubes. Compared with amorphous nanotubes, the nozzles of anatase nanotubes collapsed slightly (Figure 5e–h), but the tube diameters and

lengths kept the original values, which indicates that TiO$_2$ nanotubes obtained by anodic oxidation method have good thermal stability.
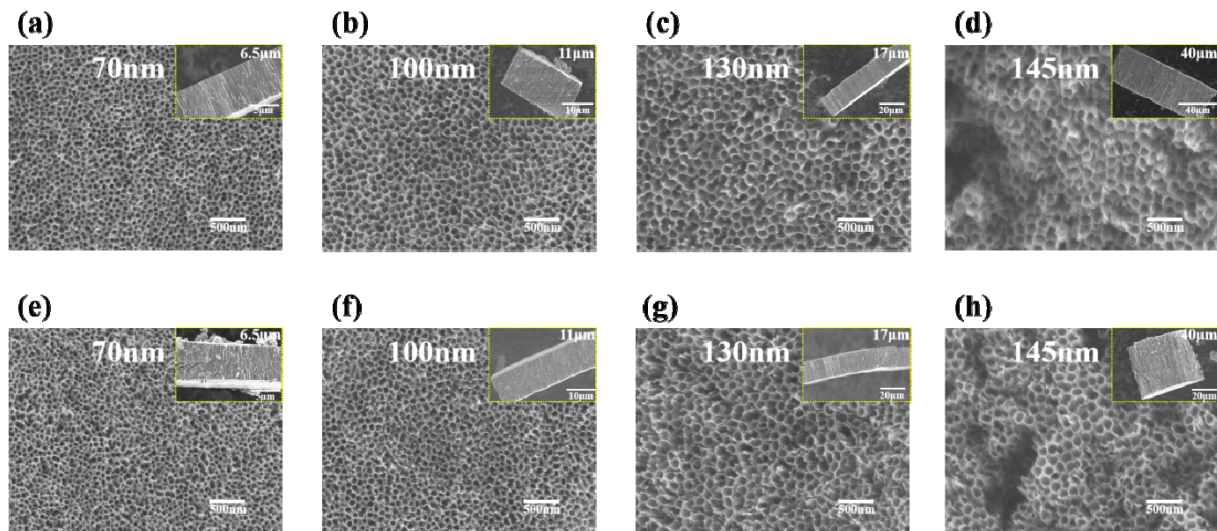

Figure 5. SEM images of top view of TiO$_2$ nanotube arrays before (**a**–**d**) and after (**e**–**h**) annealing with different oxidation times in electrolyte with 0.2 wt% NH$_4$F: (**a**,**e**) 2 h; (**b**,**f**) 5 h; (**c**,**g**) 10 h; (**d**,**h**) 20 h. Inserts show side view of TiO$_2$ nanotube arrays.

Figure 6 demonstrates the change of nanotubes under the electrolyte of 0.5 wt% NH$_4$F. The diameters and lengths of TiO$_2$ nanotubes were: 80 nm and 7.5 μm in 2 h oxidation (Figure 6a); 130 nm and 12 μm in 5 h oxidation (Figure 6b); 150 nm and 18 μm in 10 h oxidation (Figure 6c); and 160 nm and 45 μm in 20 h oxidation (Figure 6d), respectively. After annealing, nozzles collapsed slightly but the tube diameters and lengths remained the same. Similarly, the morphology of the nanotubes after annealing also kept the same (Figure 6e–h). What is exciting is that in comparison with all the above samples, the nanotube arrays obtained by anodizing at 0.5 wt% NH$_4$F for 10 h showed a high-ordered nanotube array.
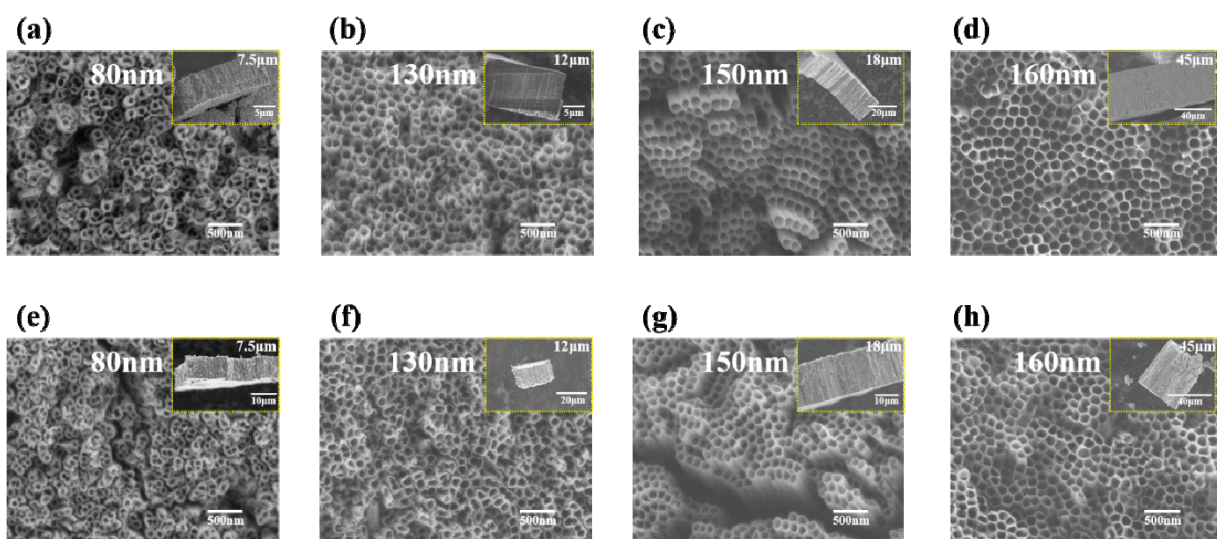

Figure 6. SEM images of top view of TiO$_2$ nanotube arrays before (**a**–**d**) and after (**e**–**h**) annealing with different oxidation times in electrolyte with 0.5 wt% NH$_4$F: (**a**,**e**) 2 h; (**b**,**f**) 5 h; (**c**,**g**) 10 h; (**d**,**h**) 20 h. Inserts show side view of TiO$_2$ nanotube arrays.

The concentration of F$^-$ ions can affect the morphology and length of the nanotube. Figure 7 exhibits the changes in the diameter and length of nanotubes with different oxidation times under two different F$^-$ concentrations. In this work, the diameter and length of the nanotubes were positively correlated with F$^-$ ion concentration and oxidation time. When the F$^-$ ion concentration was suitable, more pores were chemically etched uniformly and synchronously on the entire oxide layer surface. An excessively high fluoride ion concentration led to the rapid formation of soluble complex ions [TiF$_6$]$^{2-}$, thereby inhibiting the formation of an oxide layer and further hindering the growth of nanotubes. Low F$^-$ ion concentration resulted in the insufficient dissolution of the formed barrier layer, and the formation of a dense oxide layer [38,39]. The growth rate of nanotube diameter gradually decreased with the increase of oxidation time, while the increase in nanotube length showed an opposite trend. This was caused by the gradual decrease of the dissolution rate between the nanotubes, and more fluoride ions were used to push the nanotubes toward the titanium substrate. Obviously, the growth and dissolution of the nanotubes had not yet reached an equilibrium, which means that the nanotubes would continue to grow as the oxidation time increased.
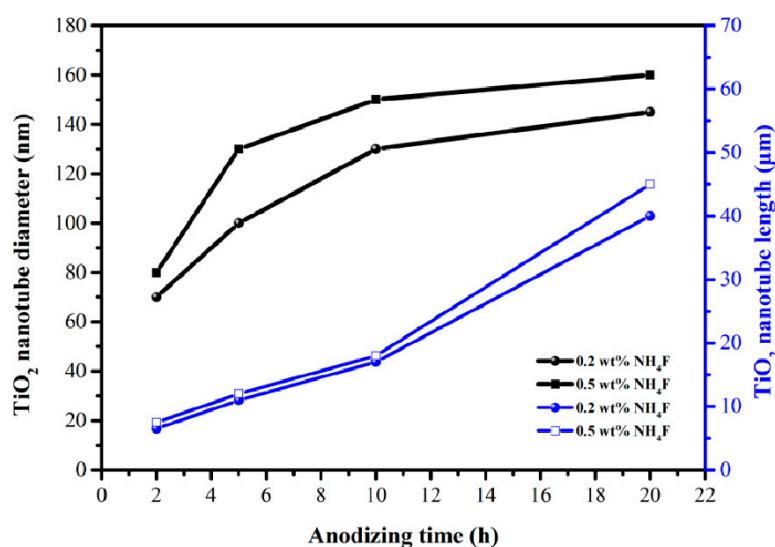

Figure 7. Comparison of TiO$_2$ nanotube diameters and lengths obtained under different anodizing times in electrolyte with 0.2 and 0.5 wt% NH$_4$F.

Owing to its sufficient capacity and higher lithiation potential (~1.6 V vs. Li/Li$^+$), TiO$_2$ is often considered as a suitable anode material [28,40,41]. The electrochemical reaction of insertion/extraction of Li$^+$ in TiO$_2$ nanotube electrodes is as follows:

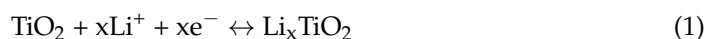$$TiO_2 + xLi^+ + xe^- \leftrightarrow Li_xTiO_2 \tag{1}$$

Figure 8a,b reveals CV curves of amorphous and anatase TiO$_2$ nanotubes. For amorphous TiO$_2$ nanotubes, there is a reduction peak around 1.1 V, which indicates that part of the TiO$_2$ has undergone a phase change to form a cubic phase of Li$_2$Ti$_2$O$_4$ [42], and it is only visible in the first cycle, proving that it is irreversible. Amorphous TiO$_2$ nanotube has mainly displayed pseudocapacitive behavior [43,44]. For anatase TiO$_2$ nanotubes, a pair of redox peaks appear around 1.6 and 2.1 V, respectively. The redox process (Ti^{4+} $\leftrightarrow$ Ti^{3+}) is accompanied by Li$^+$ insertion/extraction into the oxide structures, which represents the transition from lithium-poor phase Li$_x$TiO$_2$ to orthorhombic lithium titanite (Li$_{\sim 0.55}$TiO$_2$) [45].

Figure 8c,d shows that charge–discharge curves of amorphous TiO$_2$ nanotubes were sloping with no voltage plateau, while the curves of anatase TiO$_2$ nanotubes had two obvious plateaus at 1.78 and 1.85 V, which were consistent with CV curves. This result

indicates that no two-phase reaction occurred in the amorphous TiO_2 nanotube electrode. The plateaus in anatase TiO_2 nanotube electrode can be attributed to the insertion and extraction of Li^+ from tetrahedral and octahedral positions [46]. Amorphous TiO_2 nanotubes undergo large irreversible first discharge capacity loss, contributing to irreversible decomposition of part of the electrolyte, and changes of initial oxide morphology, and stoichiometric ratio. Anatase TiO_2 nanotube electrode showed stable charge–discharge for the initial three cycles, owing to its stable crystal structure. After the second cycle, the battery no longer had a significant loss of discharge capacity, that is, it entered a stable redox stage.
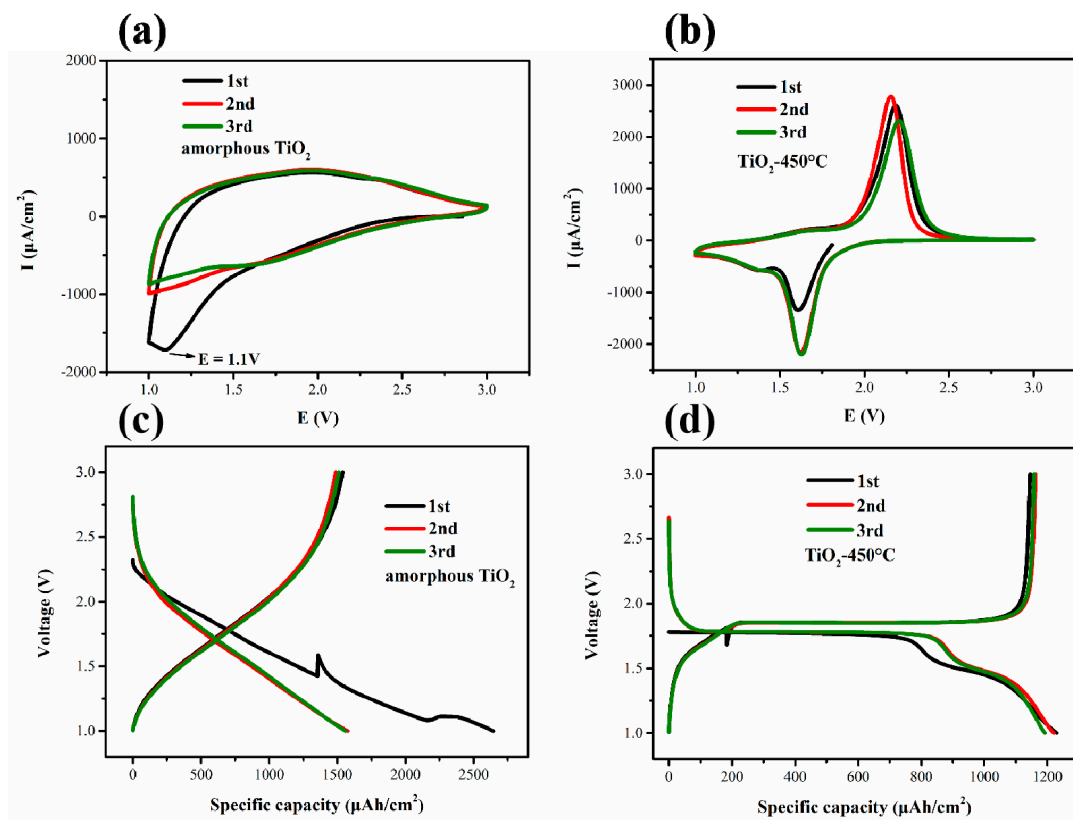

Figure 8. CV curves of amorphous TiO_2-20 h (**a**) and anatase TiO_2-20 h-450 °C (**b**) at a sweep rate of 0.2 mV/s. The first three cycles charge/discharge curves of amorphous (**c**) and anatase (**d**) TiO_2 nanotubes. The voltage range was between 1.0 and 3.0 V, and the constant charge and discharge current was 100 μA/cm². The samples were synthesized in electrolyte with 0.5 wt% NH_4F and anodization time of 20 h.

The kinetic characteristics of TiO_2 nanotube anodes were analyzed by electrochemical impedance spectroscopy (EIS). Figure 9 shows the Nyquist plots of the amorphous and anatase TiO_2 anodes prepared with different oxidation times, where R_Ω and R_{ct} correspond to electrolyte resistance and interface charge transfer resistance, respectively [47,48]. R_Ω of amorphous and anatase TiO_2 was around 5 Ω, and the value of anatase TiO_2 was slightly smaller than that of amorphous TiO_2. The R_{ct} values of amorphous TiO_2 increased greatly with the increase of the oxidation time, especially when the oxidation time was greater than 5 h. In contrast, the values of anatase TiO_2 were relatively stable. The results confirm that TiO_2 with stable crystal structure can display better kinetic performance.
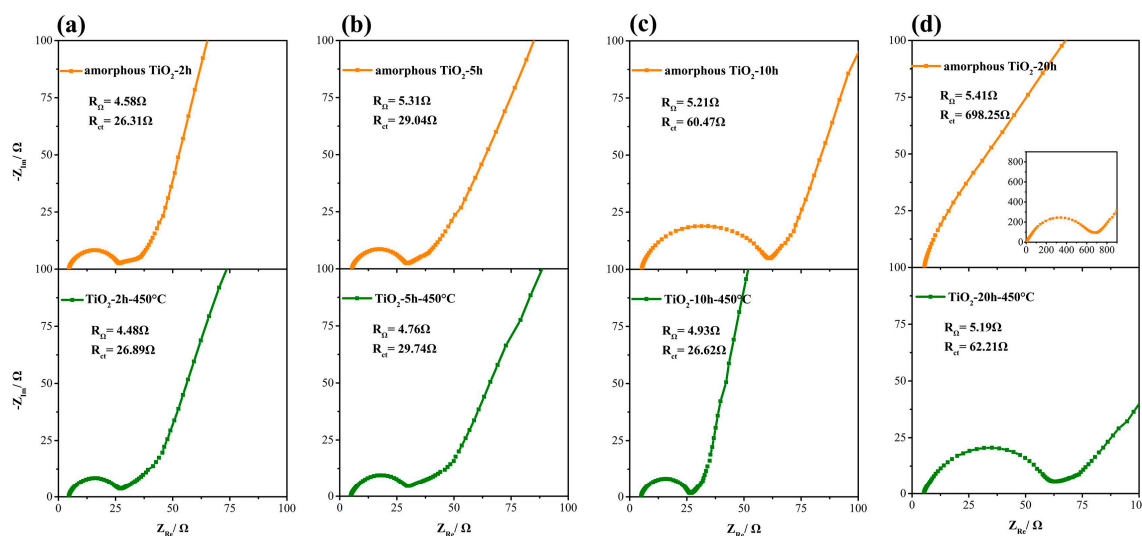
Figure 9. Nyquist plots of amorphous TiO_2-20 h and anatase TiO_2-20 h-450 °C anodes under different oxidation times: (**a**) 2 h; (**b**) 5 h; (**c**) 10 h; (**d**) 20 h. The samples were synthesized in electrolyte with 0.5 wt% NH_4F and anodization time of 20 h.

Figure 10 depicts the rate performance and cycling stability of amorphous and anatase TiO_2 nanotube electrodes. The areal capacities of amorphous TiO_2 are higher than those of anatase TiO_2, which is due to the high defects, loose structure, and disorder of amorphous TiO_2 [30]. For example, reversible capacity of amorphous TiO_2 is 1350 µAh/cm^2, while the same value of anatase TiO_2 is 1240 µAh/cm^2 for samples obtained under 0.2 wt% NH_4F and 20 h oxidation time, which is higher than TiO_2 nanotube foam with areal capacity of 507 µAh/cm^2 at 50 µA/cm^2 [30]. In comparison, the rate performance of anatase TiO_2 electrodes under different current densities was more stable than that of amorphous TiO_2. Therefore, as lithium-ion battery anodes, anatase TiO_2 nanotubes show more stable electrochemical performance than amorphous phase. The areal capacities increased with prolonging oxidation time and F^- ions concentration. With the increase of oxidation time and F^- ions concentration, longer nanotubes were formed in Ti foil, contributing to enhanced areal capacities. As shown in Table 1, with increase of the diameter and length of TiO_2 nanotubes, the specific area capacities also increased. The increased tube diameter can increase the contact area between the electrode and the electrolyte, while longer TiO_2 nanotubes can increase the amount of active materials per unit area. Therefore, TiO_2 nanotubes with larger tube diameter and longer tube length show better electrochemical performances.
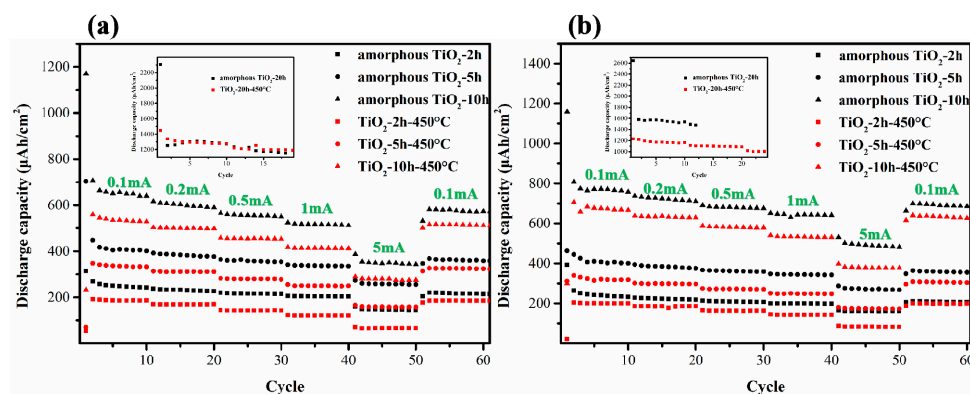

Figure 10. Cycling stability and rate performances of amorphous and anatase TiO_2 nanotubes with different anodizing times (2, 5, 10 h (inserts: 20 h)) under different current densities and different NH_4F contents in TiO_2 nanotubes growth: (**a**) 0.2 wt%, (**b**) 0.5 wt%.

Table 1. Relationship between the second discharge capacity and the diameter/length of the nanotubes.

Anodization Electrolyte	Samples	Nanotube Diameter (nm)	Nanotube Length (μm)	2nd Discharge Capacity (μAh/cm^2)
0.2 wt% NH$_4$F	TiO$_2$-2 h	70	6.5	269.1
	TiO$_2$-5 h	100	11	448.2
	TiO$_2$-10 h	130	17	705.8
	TiO$_2$-20 h	145	40	1251.1
	TiO$_2$-2 h-450 °C	70	6.5	190.4
	TiO$_2$-5 h-450 °C	100	11	347.3
	TiO$_2$-10 h-450 °C	130	17	558.8
	TiO$_2$-20 h-450 °C	145	40	1336.9
0.5 wt% NH$_4$F	TiO$_2$-2 h	80	7.5	264.1
	TiO$_2$-5 h	130	12	444.2
	TiO$_2$-10 h	150	18	808.3
	TiO$_2$-20 h	160	45	1576.1
	TiO$_2$-2 h-450 °C	80	7.5	203.2
	TiO$_2$-5 h-450 °C	130	12	339.5
	TiO$_2$-10 h-450 °C	150	18	706.3
	TiO$_2$-20 h-450 °C	160	45	1220.1

4. Conclusions

In this work, we studied the relationship between electrochemical performance and crystallographic structure of TiO$_2$ and geometry of as-formed TiO$_2$ nanotube arrays. Highly ordered TiO$_2$ nanotube arrays with a tube diameter of 70–160 nm and length of 6.5–45 μm were grown by anodic oxidation of Ti foil. With the studied growth mechanism, the diameter and length of TiO$_2$ nanotubes could be adjusted by controlling oxidation time and F$^-$ concentration. The formation of [TiF$_6$]$^{2-}$ complexes led to the chemical dissolution of formed TiO$_2$ at oxide/electrolyte interface, which favors the growth of nanotubes and increase of tube diameter. The higher the F$^-$ concentration, the larger the tube diameter. The tube length was related to the total electrical charge. Thus, the longer the reaction time, the longer the tube length. F$^-$ concentration did not affect the increase trend of tube length, but only increased the TiO$_2$ tube diameter. Serving as Li-ion battery anodes, reversible capacities of amorphous TiO$_2$-20 h and anatase TiO$_2$-20 h-450 °C were 1350 and 1240 μAh/cm^2, respectively. The higher areal capacity of amorphous TiO$_2$ was due to the high defects and loose structure of the amorphous phase. However, anatase TiO$_2$ nanotubes showed better rate performance owing to their stable crystallographic structure. Anatase TiO$_2$ nanotubes with longer tubes showed higher areal capacity and stable cycling performances. The increased tube diameter increased the contact area between the electrode and the electrolyte, and longer TiO$_2$ nanotubes increased the amount of active materials per unit area. The anodic oxidation method can be a facile nanotechnology tool to synthesize other 1D nanotube metal oxides, i.e., Nb$_2$O$_5$, Fe$_2$O$_3$, ZnO, CuO etc.

References

1. Fujishima, A.; Honda, K. Electrochemical photolysis of water at a semiconductor electrode. *Nature* **1972**, *238*, 37–38. [CrossRef] [PubMed]

2. Ganguly, P.; Kumar, S.; Muscetta, M.; Padmanabhan, N.T.; Clarizia, L.; Akande, A.; Hinder, S.; Mathew, S.; John, H.; Breen, A.; et al. New insights into the efficient charge transfer of ternary chalcogenides composites of TiO_2. *Appl. Catal. B* **2021**, *282*, 119612. [CrossRef]

3. Roy, P.; Berger, S.; Schmuki, P. TiO_2 nanotubes: Synthesis and applications. *Angew. Chem. Int. Ed.* **2011**, *50*, 2904–2939. [CrossRef] [PubMed]

4. Hou, X.L.; Aitola, K.; Lund, P.D. TiO_2 nanotubes for dye-sensitized solar cells-A review. *Energy Sci. Eng.* **2020**, 1–17. [CrossRef]

5. Rousseau, R.; Glezakou, V.A.; Selloni, A. Theoretical insights into the surface physics and chemistry of redox-active oxides. *Nat. Rev. Mater.* **2020**, *5*, 460–475. [CrossRef]

6. Sudarsanam, P.; Li, H.; Sagar, V. TiO_2-Based water-tolerant acid catalysis for biomass-based fuels and chemicals. *ACS Catal.* **2020**, *10*, 9555–9584. [CrossRef]

7. Zayat, M.; Garcai-Parejo, P.; Levy, D. Preventing UV-light damage of light sensitive materials using a highly protective UV-absorbing coating. *Chem. Soc. Rev.* **2007**, *36*, 1270–1281. [CrossRef]

8. Jiang, Z.; Xu, X.H.; Ma, Y.H.; Cho, H.S.; Ding, D.; Wang, C.; Wu, J.; Oleynikov, P.; Jia, M.; Cheng, J.; et al. Filling metal-organic framework mesopores with TiO_2 for CO_2 photoreduction. *Nature* **2020**, *586*, 549–554. [CrossRef]

9. Gao, B.; Sun, M.X.; Ding, W.; Ding, Z.P.; Liu, W.Z. Decoration of γ-graphyne on TiO_2 nanotube arrays: Improved photoelectro-chemical and photoelectrocatalytic properties. *Appl. Catal. B* **2021**, *281*, 119492. [CrossRef]

10. Gao, J.Q.; Shen, Q.Q.; Guan, R.F.; Xue, J.B.; Liu, X.G.; Jia, H.S.; Li, Q.; Wu, Y.C. Oxygen vacancy self-doped black TiO_2 nanotube arrays by aluminothermic reduction for photocatalytic CO_2 reduction under visible light illumination. *J. CO_2 Util.* **2020**, *35*, 205–215. [CrossRef]

11. Vazquez-Galvan, J.; Flox, C.; Jervis, J.R.; Jorge, A.B.; Shearing, P.R.; Morante, J.R. High-power nitrided TiO_2 carbon felt as the negative electrode for all-vanadium redox flow batteries. *Carbon* **2019**, *148*, 91–104. [CrossRef]

12. Pomerantseva, E.; Bonaccorso, F.; Feng, X.L.; Cui, Y.; Gogotsi, Y. Energy storage: The future enabled by nanomaterials. *Science* **2019**, *366*, eaan8285. [CrossRef] [PubMed]

13. Iijima, S. Helical microtubules of graphitic carbon. *Nature* **1991**, *354*, 56–58. [CrossRef]

14. Andronic, L.; Enesca, A. Black TiO_2 synthesis by chemical reduction methods for photocatalysis applications. *Front. Chem.* **2020**, *8*, 565489. [CrossRef]

15. Tsuchiyaa, H.; Schmuki, P. Less known facts and findings about TiO_2 nanotubes. *Nanoscale* **2020**, *12*, 8119–8132. [CrossRef]

16. Wu, C.W.; Ohsuna, T.; Kuwabara, M.; Kuroda, K. Formation of highly ordered mesoporous titania films consisting of crystalline nanopillars with inverse mesospace by structural transformation. *J. Am. Chem. Soc.* **2006**, *128*, 4544–4545. [CrossRef]

17. Kasuga, T.; Hiramatsu, M.; Hoson, A.; Sekino, T.; Niihara, K. Titania nanotubes prepared by chemical processing. *Adv. Mater.* **1999**, *11*, 1307–1311. [CrossRef]

18. Mor, G.K.; Shankar, K.; Paulose, M.; Varghese, O.K.; Grimes, C.A. Enhanced photocleavage of water using titania nanotube arrays. *Nano Lett.* **2005**, *5*, 191–195. [CrossRef]

19. Liang, Z.Q.; Bai, X.J.; Hao, P.; Guo, Y.C.; Xue, Y.J.; Tian, J.; Cui, H.Z. Full solar spectrum photocatalytic oxygen evolution by carbon-coated TiO_2 hierarchical nanotubes. *Appl. Catal. B* **2019**, *243*, 711–720. [CrossRef]

20. Ni, J.F.; Fu, S.D.; Yuan, Y.F.; Ma, L.; Jiang, Y.; Li, L.; Lu, J. Boosting sodium storage in TiO_2 nanotube arrays through surface phosphorylation. *Adv. Mater.* **2018**, *30*, 1704337. [CrossRef]

21. Raja, K.S.; Misra, M.; Paramguru, K. Formation of self-ordered nano-tubular structure of anodic oxide layer on titanium. *Electrochim. Acta* **2005**, *51*, 154–165. [CrossRef]

22. Macak, J.M.; Tsuchiya, H.; Schmuki, P. High-aspect-ratio TiO_2 nanotubes by anodization of titanium. *Angew. Chem. Int. Ed.* **2005**, *44*, 2100–2102. [CrossRef] [PubMed]

23. Macak, J.M.; Tsuchiya, H.; Taveira, L.; Aldabergerova, S.; Schmuki, P. Smooth anodic TiO_2 nanotubes. *Angew. Chem. Int. Ed.* **2005**, *44*, 7463–7465. [CrossRef] [PubMed]

24. Wang, K.L.; Janczarek, M.; Wei, Z.S.; Raja-Mogan, T.; Endo-Kimura, M.; Khedr, T.M.; Ohtani, B.; Kowalska, E. Morphology- and crystalline composition-governed activity of titania-based photocatalysts: Overview and perspective. *Catalysts* **2019**, *9*, 1054. [CrossRef]

25. Kaczmarek, A.; Klekiel, T.; Krasicka-Cydzik, E. Fluoride concentration effect on the anodic growth of self-aligned oxide nanotube array on Ti_6Al_7Nb alloy. *Surf. Interface Anal.* **2010**, *42*, 510–514. [CrossRef]

26. Huang, W.Q.; Xu, H.Q.; Ying, Z.R.; Dan, Y.X.; Zhou, Q.Y.; Zhang, J.J.; Zhu, X.F. Split TiO_2 nanotubes-Evidence of oxygen evolution during Ti anodization. *Electrochem. Commun.* **2019**, *106*, 106532. [CrossRef]

27. Rao, B.M.; Torabi, A.; Varghese, O.K. Anodically grown functional oxide nanotubes and applications. *MRS Commun.* **2016**, *6*, 375–396. [CrossRef]

28. Lee, K.; Mazare, A.; Schmuki, P. One-dimensional titanium dioxide nanomaterials: Nanotubes. *Chem. Rev.* **2014**, *114*, 9385–9454. [CrossRef] [PubMed]

29. Macak, J.M.; Schmuki, P. Anodic growth of self-organized anodic TiO_2 nanotubes in viscous electrolytes. *Electrochim. Acta* **2006**, *52*, 1258–1264. [CrossRef]

30. Jiang, Y.; Hall, C.; Burr, P.A.; Song, N.; Lau, D.; Yuwono, J.; Wang, D.W.; Ouyang, Z.; Lennon, A. Fabrication strategies for high-rate TiO$_2$ nanotube anodes for Li ion energy storage. *J. Power Sources* **2020**, *463*, 228205. [CrossRef]

31. Sugiawati, V.; Vacandio, F.; Galeyeva, A.; Kurbatov, A.; Djenizian, T. Enhanced electrochemical performance of electropolymerized self-organized TiO$_2$ nanotubes fabricated by anodization of Ti grid. *Front. Phys.* **2019**, *7*, 179. [CrossRef]

32. Pham, T.N.; Park, D.; Lee, Y.; Kim, T.; Hur, J.; Oh, Y.K.; Lee, Y.C. Combination-based nanomaterial designs in single and double dimensions for improved electrodes in lithium ion batteries and faradaic supercapacitors. *J. Energy Chem.* **2019**, *38*, 119–146. [CrossRef]

33. Yi, Z.; Zeng, Y.; Wu, H.; Chen, X.F.; Fan, Y.X.; Yang, H.; Tang, Y.J.; Yi, Y.G.; Wang, J.Q.; Wu, P.H. Synthesis, surface properties, crystal structure and dye-sensitized solar cell performance of TiO$_2$ nanotube arrays anodized under different parameters. *Results Phys.* **2019**, *15*, 102609. [CrossRef]

34. Albu, S.P.; Schmuki, P. Influence of anodization parameters on the expansion factor of TiO$_2$ nanotubes. *Electrochim. Acta* **2013**, *91*, 90–95. [CrossRef]

35. Jennings, J.R.; Ghicov, A.; Peter, L.M.; Schmuki, P.; Walker, A.B. Dye-sensitized solar cells based on oriented TiO$_2$ nanotube arrays: Transport, trapping, and transfer of electrons. *J. Am. Chem. Soc.* **2008**, *130*, 13364–13372. [CrossRef]

36. Su, Z.; Zhou, W. Formation, morphology control and applications of anodic TiO$_2$ nanotube arrays. *J. Mater. Chem.* **2011**, *21*, 8955–8970. [CrossRef]

37. Dong, Z.H.; Song, Y. Size-and morphology-dependent structural transformations in anatase TiO$_2$ nanowires under high pressures. *Can. J. Chem.* **2015**, *93*, 165–172. [CrossRef]

38. Shankar, K.; Mor, G.K.; Prakasam, H.E.; Yoriya, S.; Paulose, M.; Varghese, O.K.; Grimes, C.A. Highly-ordered TiO$_2$ nanotube arrays up to 220 μm in length: Use in water photoelectrolysis and dye-sensitized solar cells. *Nanotechnology* **2007**, *18*, 065707. [CrossRef]

39. Wang, X.Q.; Li, Y.F.; Song, H.; Huang, Y.D.; Su, R.; Besenbacher, F. Fluoride concentration controlled TiO$_2$ nanotubes: The interplay of microstructure and photocatalytic performance. *RSC Adv.* **2016**, *6*, 18333–18339. [CrossRef]

40. Partheeban, T.; Kesavan, T.; Jithin, A.; Dharaneshwar, S.; Sasidharan, M. Melamine-templated TiO$_2$ nanoparticles as anode with high capacity and cycling stability for lithium-ion batteries. *J. Solid State Electrochem.* **2020**. [CrossRef]

41. Wang, H.; Liang, X.; Wang, J.; Jiao, S.; Xue, D. Multifunctional inorganic nanomaterials for energy applications. *Nanoscale* **2020**, *12*, 14–42. [CrossRef] [PubMed]

42. Steiner, D.; Auer, A.; Portenkirchner, E.; Kunze-Liebhauser, J. The role of surface films during lithiation of amorphous and anatase TiO$_2$ nanotubes. *J. Electroanal. Chem.* **2018**, *812*, 166–173. [CrossRef]

43. Sugiawati, V.; Vacandio, F.; Djenizian, T. All-Solid-State Lithium Ion Batteries Using Self-Organized TiO$_2$ Nanotubes Grown from Ti-6Al-4V Alloy. *Molecules* **2020**, *25*, 2121. [CrossRef] [PubMed]

44. Liang, X.; Chen, K.; Xue, D. A Flexible and Ultrahigh Energy Density Capacitor via Enhancing Surface/Interface of Carbon Cloth Supported Colloids. *Adv. Energy Mater.* **2018**, *8*, 1703329. [CrossRef]

45. Bresser, D.; Paillard, E.; Binetti, E.; Krueger, S.; Striccoli, M.; Winter, M.; Passerini, S. Percolating networks of TiO$_2$ nanorods and carbon for high power lithium insertion electrodes. *J. Power Sources* **2012**, *206*, 301–309. [CrossRef]

46. Huo, J.; Xue, Y.; Liu, Y.; Guo, S. Low-temperature preparation of mesoporous TiO$_2$ honeycomb-like structure on TiO$_2$ nanotube arrays as binder-free anodes for lithium-ion batteries. *J. Electroanal. Chem.* **2020**, *863*, 114088. [CrossRef]

47. Jiao, S.; Xue, D. High areal capacitance of manganese oxide electrodes with cerium as rare earth modification. *Nanotechnology* **2020**, *31*, 354004. [CrossRef]

48. Liang, X.; Xue, D. Ce(OH)$_3$ as a novel negative electrode material for supercapacitors. *Nanotechnology* **2020**, *31*, 374003. [CrossRef]